remote sensing

MDPI

Article

Comprehensive Evaluation of Data-Related Factors on BDS-3 B1I + B2b Real-Time PPP/INS Tightly Coupled Integration

Junyao Kan [1,2], Zhouzheng Gao [1,*], Qiaozhuang Xu [1], Ruohua Lan [1], Jie Lv [1] and Cheng Yang [1]

[1] School of Land Science and Technology, China University of Geosciences Beijing, 29 Xueyuan Road, Beijing 100083, China
[2] Aerospace Information Research Institute, Chinese Academy of Sciences, Beijing 100094, China
* Correspondence: zz.gao@cugb.edu.cn

Abstract: Owing to the developments of satellite-based and network-based real-time satellite precise products, the Precise Point Positioning (PPP) technique has been applied far and wide, especially since the PPP-B2b service was provided by the third-generation BeiDou Navigation Satellite System (BDS-3). However, satellite outages during dynamic application lead to significant degradation of the accuracy and continuity of PPP. A generally used method is integrating PPP with Inertial Measurement Units (IMUs) to enhance positioning performance. Previous works on this topic are usually based on IMU data at a high sampling rate and are mostly implemented in post-processing mode. This paper will carry out a compressive assessment of the impacts of different types of precise satellite products (real-time products from the CAS, DLR, GFZ, WHU, and the final one from GFZ), Doppler observations, and different sampling rates of IMU data on the performance of the tightly coupled integration of the BDS-3 B1I/B2b and the Inertial Navigation System (INS). Results based on a group of on-board experimental data illustrate that (1) the positioning accuracy with products supplied by the CAS and WHU are roughly consistent with those using the final products; (2) the Doppler observations can effectively improve the accuracies of velocity, attitude, and vertical position at the initial epochs and during the reconvergence periods, but have invisible influences on the overall positioning, velocity, and attitude determination; and (3) the impact of IMU data interval on the performance of PPP/INS tightly coupled integration is insignificant when there are enough available satellites. However, the divergent speed of position is visibly affected by the IMU sampling rate during satellite outage periods.

Keywords: the third-generation BeiDou navigation satellite system (BDS-3); robust Kalman filter; real-time satellite precise products; Doppler observation; IMU data rate

Citation: Kan, J.; Gao, Z.; Xu, Q.; Lan, R.; Lv, J.; Yang, C. Comprehensive Evaluation of Data-Related Factors on BDS-3 B1I + B2b Real-Time PPP/INS Tightly Coupled Integration. *Remote Sens.* **2022**, *14*, 6395. https://doi.org/10.3390/rs14246395

Academic Editor: Giuseppe Casula

Received: 22 November 2022
Accepted: 15 December 2022
Published: 18 December 2022

1. Introduction

The emerging applications such as autonomous driving and smart cities present an increasingly urgent demand for high-precision and high-frequency spatial–temporal data information in real time. The Precise Point Positioning (PPP) technique [1,2], which requires only a single receiver, can accomplish centimeter-level positioning worldwide with the advantages of flexibility and effective cost. Currently, PPP based on multi-constellation Global Navigation Satellite System (GNSS) observations has emerged as a powerful platform for offering high-accuracy location services because of the merits of global coverage and all-weather as well as non-accumulative positioning error [3]. Meanwhile, the performance of PPP relies heavily on the accuracy of satellite orbit and clock products [4]. The International GNSS Service (IGS) Analysis Centers (ACs) supply these products to users, which can be divided into three types, namely ultra-rapid products, rapid products, and final products. Due to the latencies of rapid and final products, they are inapplicable for real-time applications. Although ultra-rapid products are capable of accomplishing real-time positioning, their positioning performance is poor [5,6]. To meet the increasing

requirement for real-time high-precision positioning and applications, IGS established the Real-Time Pilot Project (RTPP), and the Real-Time Service (RTS) was officially operated in 2013. Based on the NTRIP (Networked Transport of RTCM via Internet Protocol), the real-time orbit and clock products in the form of State Space Representation (SSR) are supplied worldwide by way of the Internet [7,8]. At present, there are several ACs that provide real-time product streams, for instance, BKG (Bundesamt für Kartographie und Geodäsie), DLR (Deutsches zentrum für Luft- und Raumfahrt), the CNES (National Centre for Space Studies), the ESA (European Space Agency), GFZ (GeoForschungsZentrum), WHU (Wuhan University), GMV (GMV Aerospace and Defense), and the CAS (Chinese Academy of Sciences). In recent years, the qualities of GNSS real-time and post-precise products have been validated by numerous scholars [9,10]. The accuracy of real-time satellite orbit and clock products of GPS, Galileo, GLONASS, and BDS-2 from the CNES has been evaluated in [11]. The experiment results show that the GPS products can provide the PPP solutions within 15 cm, where the orbit errors are 5 cm and the clock errors are 0.3 ns. In contrast, GPS products are the highest accuracy among the four systems. Similar conclusions can also be found in [12]. In [13], the accuracies of SSR products supplied by the ACs including the IGS, BKG, DLR, GFZ, the ESA, GMV, the CNES, and the CAS were assessed. Numerical results suggested that the PPP solutions based on the real-time products required practically the identical convergence time (about 20–30 min) as those utilizing final products to obtain the same positioning accuracy grade (10–15 cm). Some scholars also analyzed the positioning performance based on final precision products [14]. The multi-GNSS precise satellite orbit and clock products supplied by ACs of the ESA, GFZ, WHU, and the CODE (Center for Orbit Determination in Europe) were studied. Relevant outcomes proved that distinctions among ACs' precise products were slighter. Therein, precise products from GFZ perform with higher accuracy around the Europe area, and the products from the CODE are more accurate around the China region.

The above research evaluated the accuracy of satellite orbits and clocks and their impacts on positioning in the field of accuracy and convergence time of PPP. Extensive works have shown that the PPP depending on real-time SSR corrections has the potential to be applied in many fields. However, there are challenging environments (tunnels, urban canyons, and viaducts, for instance) around where satellites' signals will be blocked. Such conditions make it hard to obtain continuous and reliable positioning results by using GNSS measurements only. To overcome the drawbacks of GNSS, the Inertial Navigation System (INS), which can maintain a stand-alone solution by using the measurements of carrier motion from the Inertial Measurement Unit (IMU), is employed. The IMU data, which will not be affected by the surrounding environments, can cover the shortage of the GNSS during signal-outage environments. Currently, the GNSS/INS tightly coupled integration (TCI), directly integrating GNSS observations with the INS-predicted values, can work well during GNSS satellite partial-outage periods [15–17]. In recent decades, many works have been conducted on PPP/INS TCI, and it can provide decimeter positioning accuracy even when GNSS signals are partially or entirely interrupted [18–20]. Since the technology of the Micro-Electro-Mechanical-System (MEMS) sensor has made significant advances, various studies were conducted to investigate the integration with PPP and MEMS INS [21–25]. The works in [21] showed that the PPP/MEMS INS TCI could provide decimeter positioning accuracies. The study of integrating GPS PPP with a MEMS-based inertial system in [22] inferred that decimeter-level positioning accuracy can still be attained despite the GPS signal having outages of 30 s. A new approach that the multi-GNSS PPP and MEMS IMUs are integrated tightly at the observation level is proposed in [23]. The corresponding results illustrated that the multi-GNSS and INS could heighten the performance of PPP in the fields of precision and convergence time. These listed works mainly verified the performances of PPP/INS integration in the post-processing mode. In [26], an integration algorithm of GPS + Galileo PPP and a MEMS-based INS was applied in real-time mode. The real-time products from the CNES are saved beforehand, which are utilized to make the simulation of real-time situations. The outcomes reveal that the positioning accuracy can

maintain centimeter grade under open sky environments, and the positioning accuracy can maintain decimeter level when there are 10 to 60 s of GNSS outages. The consumer-level IMUs are currently widely used in many practical applications, such as unmanned aerial vehicle (UAV) navigation and vehicle-borne navigation [27–29]. The work in [29] presents a real-time loose integration between single-frequency PPP and a low-cost consumer-grade INS. The outcomes indicate that the positioning results could maintain lane-level accuracy by this real-time PPP/INS system despite passing bridges or overpasses on the road. However, the impact of real-time products from different ACs on PPP/INS tight integration has not yet been investigated. In addition, the observation of Doppler is widely used in GNSS velocity determination [30,31], and Doppler observations are often used in the TCI models [32–34], but their influence on TCI performance is rarely analyzed. To improve the PPP/INS solutions in complex environments, the Robust Kalman Filter (RKF) is introduced [34–37]. A adaptive Robust Kalman Filter for a MEMS/GNSS integrated system is designed in [37], and a vehicular experiment shows that this algorithm could constructively suppress the error divergence.

However, the above works are based on the high rate of IMU data. Although the high sampling rate of IMUs can provide more positioning solutions in detail, it also imposes a certain burden on data storage that does not meet the application requirements of the consumer-level market in real time. Applications such as pedestrian navigation demand real-time, continuous, and accurate positioning with low-cost sensors, small data storage, and non-time-consuming operation. The aim of this work is to analyze the impacts of the data-related factors such as IMU data rate, Doppler observation, real-time SSR products, and robust algorithm on real-time PPP/INS tight coupled integration. Therefore, this contribution makes a comprehensive evaluation through a set of low-cost vehicle-borne BDS-3/IMU data collected in complex environments. In addition, since the B2b signals have been publicly broadcast, the BeiDou 3 navigation services have new signal selection, and B2b signals are the same accuracy as other signals in terms of position, velocity, and timing [38,39]. In this work, we utilized the combination of B1I and B2b. The conclusions of this contribution will be conducive to the selection of data and processing strategies in practical applications, so as to obtain more efficient and accurate navigation results.

2. Methods

In this subsection, the methods of undifferenced uncombined BDS-3 PPP/INS tight integration and the Robust Kalman Filter are described in detail.

2.1. Observation Models

The measurement model can be expressed as

$$z_k = H_k x_k + \eta_k, \eta_k \sim N(0, R_k) \tag{1}$$

where z_k refers to the measurement error vector at epoch k; x_k indicates the state parameter vector; H_k is the design matrix; η_k stands for the observation noise vector; and R_k represents the corresponding covariance matrix.

The measurement error vector is formed by making the difference between BDS-3 measurements M_{GNSS} and the INS-predicted measurements $\widetilde{M}_{INS}$ [40]

$$\begin{aligned} z_k &= M_{GNSS} - \widetilde{M}_{INS} \\ &= \begin{bmatrix} P_j \\ L_j \\ D_j \end{bmatrix} - \begin{bmatrix} \left|p^s - p_{INS} - \Delta p_{INS,l}\right| + c(t_r - t^s) + b_{r,j} - b_j^s + I_{r,j}^s + T_r^s + \Delta\delta P_j \\ \left|p^s - p_{INS} - \Delta p_{INS,l}\right| + c(t_r - t^s) + \lambda_j N_j - I_{r,j}^s + T_r^s + \Delta\delta L_j \\ \left|v^s - v_{INS} - \Delta v_{INS,l}\right| + c(\dot{t}_r - \dot{t}^s) + \Delta\delta D_j \end{bmatrix} \end{aligned} \tag{2}$$

where original GNSS observations at frequency j including pseudo-range, carrier phase, and Doppler are represented as P, L, and D; p^s and v^s denote the satellite position and velocity provided by precise orbit products; p_{INS} and v_{INS} are the position and velocity

at the IMU sensor center calculated by INS; t_r and t^s represent the clock residual error of receiver and satellite; $I^s_{r,j}$ and T^s_r refer to the ionospheric and the tropospheric delay on the signal path; $b_{r,j}$ and b^s_j indicate Differential Code Biases (DCB) for receivers and satellites; N_j denotes the integer ambiguity; λ_j stands for the wavelength of carrier phase; c refers to the velocity of light; '$\cdot$' represents a variation; and $\Delta\delta P_j$, $\Delta\delta L_j$, and $\Delta\delta D_j$ refer to the sum of other error modifications, which can be obtained from appropriate error correction models for these three types of observations. Because the GNSS receiver observing center does not coincide with the IMU sensor's center, $\Delta p_{INS,l}$ and $\Delta v_{INS,l}$ are used to describe the lever arm for position and velocity, which can be written as

$$\begin{pmatrix} \Delta p_{INS,l} \\ \Delta v_{INS,l} \end{pmatrix} = \begin{pmatrix} C^e_n C^n_b l^b \\ C^e_n [(\omega^n_{in}\times) C^n_b l^b + C^n_b (l^b \times) \omega^b_{ib}] \end{pmatrix} \tag{3}$$

where l^b represents the lever arm surveyed in b-frame, which is generally measured before the experiment and utilized to calibrate the inconsistency between the GNSS receiver observing center and IMU sensor's center; C^e_n is the conversion matrix from the navigation frame (n-frame) to the earth frame (e-frame); C^n_b denotes the conversion matrix between n-frame and body frame (b-frame); ω^n_{in} indicates the angular rotation rates of n-frame relative to the inertial frame (i-frame) projected in n-frame; and ω^b_{ib} represents the angular speed in b-frame.

For the TCI model, the related state parameters used in our work can be written as

$$x_k = [\delta p^n_{INS}, \delta v^n_{INS}, \delta\Psi, \delta b_a, \delta b_g, \delta s_a, \delta s_g, \delta t_r, \dot{\delta t_r}, \delta d_{wet}, \delta dcb_r, \delta N_1, \delta N_2, \delta I_r]^T \tag{4}$$

where δp^n_{INS}, δv^n_{INS}, and $\delta\Psi$ are the error vectors of position, velocity, and attitude in the n-frame, respectively; δb_a and δs_a represent the bias error and scale factor error of the accelerometers; and δb_g and δs_g represent the corresponding errors of the gyroscopes. The rest of the state parameters are the elements related to GNSS, including receiver clock error δt_r receiver clock drift error $\dot{\delta t_r}$ wet zenith delay error δd_{wet}, receiver DCB error δdcb_r ambiguity errors δN_1 and δN_2 on frequencies L1 and L2, as well as ionospheric error δI_r.

Subsequently, H_k can be obtained by making an error perturbation operation on the innovation vector in Equation (2) around the initial state parameters provided by the INS, which indicates the designed coefficient matrix. For dual-frequency observations (f_1 and f_2), the corresponding H_k can be expressed as

$$H_k = \begin{bmatrix} H_{P_1} \\ H_{P_2} \\ H_{L_1} \\ H_{L_2} \\ H_{D_1} \\ H_{D_2} \end{bmatrix} = \begin{bmatrix} H_{INS,P} & H_{GNSS,P1} \\ H_{INS,P} & H_{GNSS,P2} \\ H_{INS,L} & H_{GNSS,L1} \\ H_{INS,L} & H_{GNSS,L2} \\ H_{INS,D} & H_{GNSS,D} \\ H_{INS,D} & H_{GNSS,D} \end{bmatrix} \tag{5}$$

$$H_{INS,P} = H_{INS,L} = \begin{bmatrix} AC_1 & 0 & AC_1\left(C^b_n l^b \times\right) & 0 & 0 & 0 & 0 \end{bmatrix} \tag{6}$$

$$H_{INS,D} = \begin{bmatrix} AD^{-1}C_1 & AC^e_n & H_{v,\Psi} & 0 & -AC^e_n C^n_b \left(l^b \times\right) & 0 & -AC^e_n H_1 diag\left(\omega^b_{ib}\right) \end{bmatrix} \tag{7}$$

$$H_{GNSS,P1} = \begin{bmatrix} H_1 & 0 & M_{wet} & H_1\beta & 0 & 0 & -E \end{bmatrix} \tag{8}$$

$$H_{GNSS,P2} = \begin{bmatrix} H_1 & 0 & M_{wet} & H_1\alpha & 0 & 0 & -\gamma E \end{bmatrix} \tag{9}$$

$$H_{GNSS,L1} = \begin{bmatrix} H_1 & 0 & M_{wet} & 0 & E & 0 & E \end{bmatrix} \tag{10}$$

$$H_{GNSS,L2} = \begin{bmatrix} H_1 & 0 & M_{wet} & 0 & 0 & E & \gamma E \end{bmatrix} \tag{11}$$

$$H_{GNSS,D1} = H_{GNSS,D2} = \begin{bmatrix} 0 & H_1 & 0 & 0 & 0 & 0 & 0 \end{bmatrix} \tag{12}$$

$$H_1 = [1, \cdots, 1]^T \tag{13}$$

$$H_{v,\Psi} = AD^{-1}C_2\left(C_n^b l^b \times\right) - AC_n^e\left[(\omega_{en}^n \times + \omega_{in}^n \times)H_1 + C_b^n\left(l^b \times \omega_{ib}^b\right)\times\right] \quad (14)$$

where A represents the direction cosine matrix of the satellite-receiver; C_1 stands for the transition matrix to transform position corrections between e-frame and n-frame; D^{-1} refers to the transition matrix to convert the lever arm from the n-frame to e-frame; E denotes the identity matrix; M_{wet} represents the mapped function of the tropospheric wet delay; $\alpha = f_1^2/(f_1^2 - f_2^2)$ and $\beta = f_2^2/(f_1^2 - f_2^2)$ are the coefficient for the ionosphere-free combination; and $\gamma = f_1^2/f_1^2$ indicates the conversion coefficient of ionospheric delay.

A prior constraint should be applied on the slant ionospheric delay in the undifferenced uncombined PPP/INS TCI model [41]. In this case, the corresponding measurement error vector z_{I_1} and the designed coefficient matrix H_{I_1} are described as

$$z_{I_1} = 40.28 \cdot STEC/f_1^2 - I_{INS} \quad (15)$$

$$H_{I_1} = [0 \;\; 0 \;\; 0 \;\; 0 \;\; 0 \;\; 0 \;\; 0 \;\; 0 \;\; 0 \;\; 0 \;\; 0 \;\; 0 \;\; 0 \;\; I] \quad (16)$$

In addition, the prior variance matrix of observation R_k can be written as

$$R_k = diag\left(R_{P_1} \; R_{P_2} \; R_{L_1} \; R_{L_2} \; R_{D_1} \; R_{D_2} \; R_{I_1}\right) \quad (17)$$

where the a priori variance of pseudo-range, carrier phase, and Doppler are decided by the satellite elevation-dependent weight function [41,42]

$$\sigma^2 = \begin{cases} {\sigma_0}^2, SA \geq \pi/6 \\ {\sigma_0}^2/(2\sin(E)), SA < \pi/6 \end{cases} \quad (18)$$

where SA and σ_0^2 are satellite elevation angle and the corresponding prior variance. The initial prior covariance of code, phase, and Doppler are set to 0.3 m, 0.003 m, and 0.1 m/s [23].

2.2. State Models

The state function of PPP/INS tight integration is shown below:

$$x_k = \Phi_{k,k-1}x_{k-1} + \mu_{k-1}, \mu_{k-1} \sim N(0, Q_{k-1}) \quad (19)$$

where $\Phi_{k,k-1}$ denotes the state transition matrix determined by the dynamics model of the state vectors mentioned above; μ_{k-1} represents the state noise vector with the a priori variance Q_{k-1}. For describing the dynamic variations of position, velocity, and attitude, the so-called PSI angle model [43] is adopted as

$$\left.\begin{array}{c} \delta\dot{\boldsymbol{p}}^c = -\boldsymbol{\omega}_{ec}^c \times \delta\boldsymbol{p}^c + \delta\boldsymbol{v}^c \\ \delta\dot{\boldsymbol{v}}^c = \boldsymbol{f}^c \times \boldsymbol{\psi} + \boldsymbol{C}_b^p \delta\boldsymbol{f}^b - \left(\boldsymbol{\omega}_{ie}^c + \boldsymbol{\omega}_{ic}^c\right) \times \delta\boldsymbol{v}^c + \delta\boldsymbol{g}^c \\ \dot{\boldsymbol{\psi}} = -\boldsymbol{\omega}_{ic}^c \times \boldsymbol{\psi} - \boldsymbol{C}_b^p \delta\boldsymbol{\omega}_{ib}^b \end{array}\right\} \quad (20)$$

where $\delta\boldsymbol{p}^c$, $\delta\boldsymbol{v}^c$, and $\boldsymbol{\psi}$ indicate the position, velocity, and attitude error in the computing frame (c-frame), respectively. In the PSI angle model, there exists a rotation vector ($\boldsymbol{\psi}$) to describe the orientation difference between the platform frame (p-frame) and the c-frame. On the basis of this, INS error analysis can be performed: $\boldsymbol{\omega}_{ec}^c$ denotes the angular rotation rate projection in c-frame of the c-frame to e-frame; $\delta\boldsymbol{g}^c$ indicates the gravity error in c-frame; $\boldsymbol{\omega}_{ie}^c$ stands for the angular rate projection in c-frame of e-frame relative to i-frame; "$\times$" represents the cross-product; $\boldsymbol{f}^c$ is the specific force from accelerometers; $\boldsymbol{C}_b^p$ refers to the attitude direction cosine matrix between b-frame and p-frame; and $\delta\boldsymbol{\omega}_{ib}^b$ and $\delta\boldsymbol{f}^b$ are the sensor errors of accelerometers and gyroscopes. Additionally, the residuals of IMU sensor

errors are decided by the first-order Gauss–Markov function [43], and the discrete-time mode is described by

$$\begin{bmatrix} \delta b_k \\ \delta s_k \end{bmatrix} = \begin{bmatrix} \exp(-\Delta t/T_b)\delta b_{k-1} \\ \exp(-\Delta t/T_s)\delta s_{k-1} \end{bmatrix} + \begin{bmatrix} \omega_{b,k} \\ \omega_{s,k} \end{bmatrix} \tag{21}$$

where T_b and T_s are the correlation time of IMU sensor errors (bias and scale factor error); Δt is the time internal; and $\omega_{b,k}$ and $\omega_{s,k}$ are the corresponding driving white noise.

For the parameters related to BDS-3, the models established by Brown and Hwang are applied to define the driving noise of the receiver clock offsets and the clock drift [44]:

$$\delta t_{r,k} = \delta t_{r,k-1} + \delta \dot{t}_{r,k-1}\Delta t + \omega_{t_{r,k-1}}, \omega_{t_{r,k-1}} \sim N\left(0, 0.5Ac^2h_0\Delta t\right) \tag{22}$$

$$\delta \dot{t}_{r,k} = \delta \dot{t}_{r,k-1} + \omega_{\dot{t}_{r,k-1}}, \omega_{\dot{t}_{r,k-1}} \sim N\left(0, 2Ac^2h_2\pi^2\Delta t\right) \tag{23}$$

where A is the experiential amplification factor; h_0 and h_2 represent the instability of the BDS-3 receiver crystal oscillator; and Δt denotes the sampling interval. Meanwhile, the random walk process is utilized to describe the dynamic noise of the zenith delay residual in the wet component, the receiver hardware time delays, and the ionospheric delays, which are adopted as

$$\delta d_{wet,k} = \delta d_{wet,k-1} + \omega_{d_{wet,k-1}}, \omega_{d_{wet,k-1}} \sim N\left(0, q^2_{d_{wet}}\Delta t\right) \tag{24}$$

$$\delta dcb_{r,k} = \delta dcb_{r,k-1} + \omega_{dcb_{r,k-1}}, \omega_{dcb_{r,k-1}} \sim N\left(0, q^2_{dcb}\Delta t\right) \tag{25}$$

$$\delta I_{r,k} = \delta I_{r,k-1} + \omega_{I_{r,k-1}}, \omega_{I_{r,k-1}} \sim N\left(0, \sigma^2_{I_{r,k-1}}\right) \tag{26}$$

where the Power Spectral Density (PSD) $q_{d_{wet}}$ is utilized to represent the dynamic noise of zenith wet delay; q_{dcb} denotes the dynamic noise of receiver DCB; and $\sigma^2_{I_{r,k-1}}$ stands for the prior noise variance of ionospheric delay. The changes in ambiguities adopt the random constant model. Then, the transition matrix $\Phi_{k,k-1}$ together with the a priori variance Q_{k-1} can be achieved.

2.3. Robust Kalman Filter

In this contribution, the RKF is adopted. Under the Extended Kalman Filter (EKF) [45,46], the observation update proceeding can be represented as

$$x_k = x_{k,k-1} + K_k(z_k - H_k x_{k,k-1}) \tag{27}$$

$$P_k = (I - K_k H_k)P_{k,k-1}(I - K_k H_k)^T + K_k R_k K_k^T \tag{28}$$

$$K_k = P_{k,k-1}H_k^T\left(H_k P_{k,k-1}H_k^T + R_k\right)^{-1} \tag{29}$$

where P_k indicates the posterior covariance matrix of the state parameters x_k; K_k denotes the Kalman gain matrix.

Nevertheless, the EKF has difficulty dealing with the observation with gross errors during the actual applications. Therefore, an RKF is utilized to eliminate the effect of measurement outliers on parameter estimation. For the low-quality or gross observations, the variance of measurement is adjusted by the robust factor:

$$\overline{R}_k = \alpha^{-1}R_k \tag{30}$$

where $\overline{R}_k$ refers to the modified measurement covariance matrix; α indicates the robust factor, which can be obtained by the IGG-III model as [46]

$$\alpha_i = \begin{cases} 1, |\widetilde{v}_i| \le k_0 \\ \frac{k_0}{|\widetilde{v}_i|}\left(\frac{k_1 - |\widetilde{v}_i|}{k_1 - k_0}\right), k_0 \le |\widetilde{v}_i| \le k_1 \\ 0, |\widetilde{v}_i| \ge k_1 \end{cases} \tag{31}$$

where k_0 and k_1 stand for the empirical constants with the values of k_0 setting to 1.0–1.5 and that of k_1 setting to 2.5–8.0; the standardized residual is adopted as $|\widetilde{v}_i| = |v_i|/\sigma_{v_i}$; and σ_{v_i} is the variance of v_i. The observation residuals vector and corresponding variance can be obtained by

$$V_k = Z_k - H_k X_k \tag{32}$$

$$P_k = R_k + H_k P_k H_k^T \tag{33}$$

where symbols are the same as those mentioned above. As shown in the above functions, the value of the robust factor is set to 1 when $|\widetilde{v}_i|$ is lower than k_0, which represents that observations are of good quality. On the other hand, the residuals will be regarded as gross errors when $|\widetilde{v}_i|$ is higher than k_1, and the weight of gross observation takes the value of zero. Nevertheless, a pimping value is adopted to avoid a singular equivalent variance matrix in the actual data processing. Then, the fresh formula of the Kalman gain can be expressed as

$$\widetilde{K}_k = P_{k,k-1} H_k^T \left(H_k P_{k,k-1} H_k^T + \overline{R}_k\right)^{-1} \tag{34}$$

Finally, the state parameters as well as the corresponding covariance matrix can be determined as

$$x_k = x_{k,k-1} + \widetilde{K}_k (z_k - H_k x_{k,k-1}) \tag{35}$$

$$P_k = \left(I - \widetilde{K}_k H_k\right) P_{k,k-1} \left(I - \widetilde{K}_k H_k\right)^T + \widetilde{K}_k \overline{R}_k \widetilde{K}_k^T \tag{36}$$

3. Experiments and Data Processing Schemes

To investigate the performance of the BDS PPP/INS TCI, a set of vehicle-borne experiments was arranged in Beijing on 23 December 2021. Figure 1 displays the detailed trajectory of the experiments. The main purpose of this work is to make a comprehensive evaluation of data-related factors on PPP/INS tight integration. Hence, the test was conducted on (1) the impact of real-time orbit and clock products from different ACs on the BDS TCI; (2) the impact of Doppler observation on the BDS TCI; (3) the impacts of the IMU sampling rate on the TCI results. As a comparison, the solutions based on GPS data are also presented. In these tests, the dual-frequency BDS (B1I/B2b) and GPS (L1/L2) measurements were collected by a NovAtel GNSS receiver with a sampling rate of 1 Hz. The accelerations and angular rotations were provided by a low-cost IMU INS616 at 100 Hz. The relevant parameters of the IMU sensor are presented in Table 1. Figure 2 displays the number of available satellites and the PDOP values for BDS-3 and GPS. It is noticeable that the observational conditions are poor during 368,732 s–371,500 s, where frequent signal partial and complete outages happen.

Table 1. Details of consumer-grade IMU sensor.

Parameters	Values
Gyroscope bias ($^\circ/h$)	2
Accelerometer bias (mGal)	40
Angular random walk ($^\circ/\sqrt{h}$)	0.15
Velocity random walk ($m/s/\sqrt{h}$)	0.05

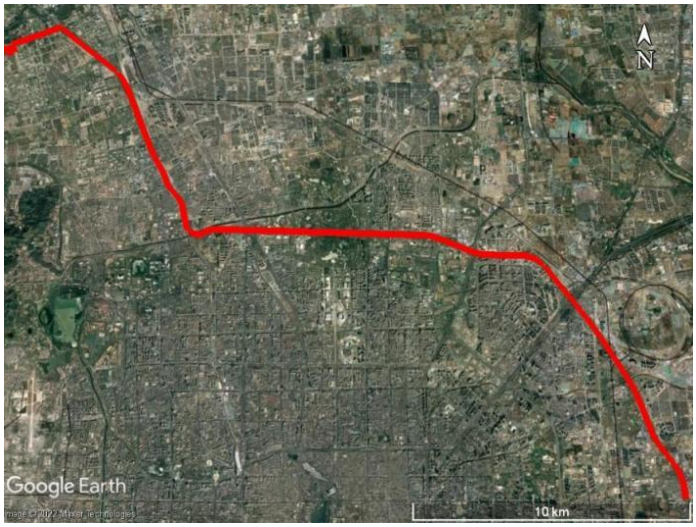

Figure 1. Trajectory of the vehicle test.

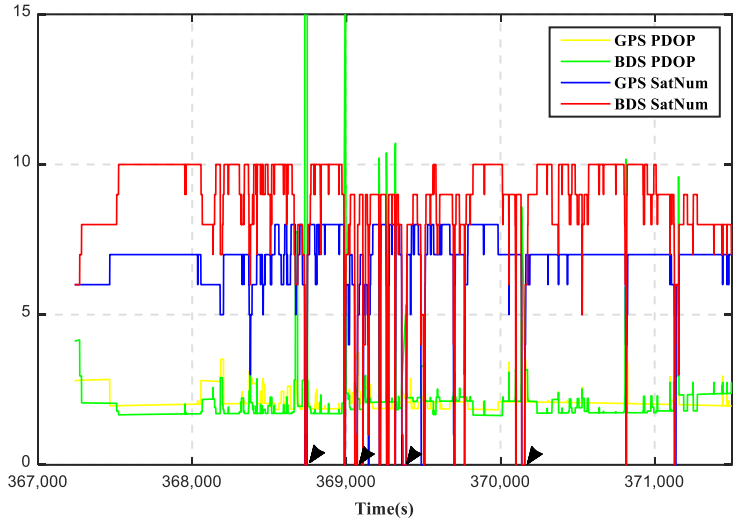

Figure 2. Number of available satellites and the corresponding PDOP.

The real-time product streams from four ACs (the CAS, DLR, GFZ, and WHU) were received. During the experiment, these data streams were decoded in real time and stored in files. As a reference, the final precision products from GFZ were also used. The raw observations were also processed in two distinct modes, namely TCI with Doppler observations (TCI-dmode0) and TCI without Doppler observations (TCI-domde1). We selected four periods of reconvergence, as pointed by black arrows in Figure 2, to further analyze the influence of Doppler observations during reconvergence periods. In addition, the raw 100 Hz IMU data were re-sampled to 50 Hz and 10 Hz, respectively. Then, the same TCI mode was adopted to process the BDS-3/GPS data and these IMU data with different sampling rates to investigate further the impacts of IMU sampling rate on the performance of positioning, velocity, and attitude determination. The specific differences between different schemes are shown in Table 2. The RTK/INS tight integration solutions calculated by Inertial Explorer (IE) software were adopted as reference values for the above schemes.

Table 2. Specific differences between different schemes.

Schemes	EKF	RKF	Final Products	Real-Time Products	With Doppler	Without Doppler	IMU Data Rate
PPP	–	–	√	–	–	–	–
TCI	√	–	√	–	√	–	100 Hz
TCI-RKF	–	√	√	–	√	–	100 Hz
RT-CAS	–	√	–	CAS	√	–	100 Hz
RT-WHU	–	√	–	WHU	√	–	100 Hz
RT-GFZ	–	√	–	GFZ	√	–	100 Hz
RT-DLR	–	√	–	DLR	√	–	100 Hz
TCI-dmode0	–	√	√	–	√	–	100 Hz
TCI-dmode1	–	√	√	–	–	√	100 Hz
TCI-100 Hz	–	√	√	–	√	–	100 Hz
TCI-50 Hz	–	√	√	–	√	–	50 Hz
TCI-10 Hz	–	√	√	–	√	–	10 Hz

4. Discussions

The impacts of real-time SSR products, robust algorithm, Doppler observation, and IMU data rate on real-time PPP/INS tightly coupled integration are presented in this section in detail.

4.1. Impacts of SSR Products and Robust Algorithm on PPP/INS Integration

This section shows the impacts of satellite SSR products and robust algorithm on BDS-3-based positioning accuracy. Figure 3 displays the position differences of BDS-3/GPS PPP, PPP/INS TCI, and the TCI-RKF based on final precise products in comparison with the reference values. The position accuracies under Root Mean Square (RMS) values are present in Tables 3 and 4. The results reveal that the solutions of PPP/INS TCI outperform the solution of PPP. Compared with TCI, the results of TCI with the RKF are slightly improved. The BDS-3 PPP RMSs are 0.882 m, 1.361 m, and 1.311 m in the east, north, and up orientations, while the BDS-3 TCI position RMSs are 0.432 m, 0.464 m, and 0.838 m, with the enhancement percentages of 51.0%, 65.9%, and 36.1%, respectively. For the BDS-3 TCI-RKF, the corresponding RMSs are 0.406 m, 0.419 m, and 0.782 m, which have slight improvement compared to BDS-3 TCI, with a gain of 6.0%, 9.7%, and 5.6% in the three directions. Similarly, the position results of GPS TCI are 0.316 m, 0.396 m, and 0.769 m, which can provide about 46.1%, 26.5%, and 21.8% position improvements to GPS PPP. These modifications from the GPS TCI-RKF are 53.9%, 65.9%, and 36.1%.

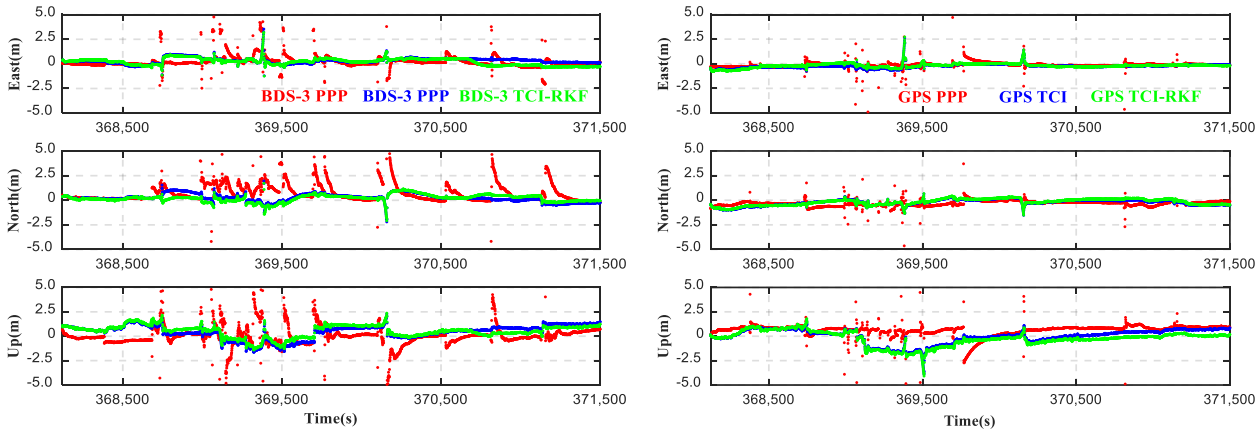

Figure 3. Position differences of PPP, PPP/INS TCI, and TCI-RKF: (**a**) position differences of BDS-3 PPP, TCI, and TCI-RKF; (**b**) position differences of GPS PPP, TCI, and TCI-RKF.

Table 3. Position RMS of BDS-3 PPP and PPP/INS TCI with different products.

Mode	BDS-3						
	PPP	TCI					
	Final	Final	Final -Robust	RT-CAS	RT-WHU	RT-GFZ	RT-DLR
East (m)	0.882	*0.432*	***0.406***	*0.383*	*0.464*	*0.572*	*1.576*
North (m)	1.361	*0.464*	***0.419***	*0.476*	*0.433*	*0.407*	*0.766*
Up (m)	1.311	*0.838*	***0.782***	*0.790*	*0.861*	*0.908*	*1.414*

Table 4. Position RMS of GPS PPP and PPP/INS TCI with different products.

Mode	GPS						
	PPP	TCI					
	Final	Final	Final -Robust	RT-CAS	RT-WHU	RT-GFZ	RT-DLR
East (m)	0.586	*0.316*	***0.305***	*0.385*	*0.334*	*0.408*	*0.320*
North (m)	0.539	*0.396*	***0.372***	*0.450*	*0.443*	*0.477*	*0.646*
Up (m)	0.984	*0.769*	***0.758***	*0.889*	*0.938*	*1.01*	*1.387*

Afterward, we further analyzed the BDS-3/GPS PPP/INS TCI position solutions using real-time SSR products from the CAS, DLR, GFZ, and WHU. The time series of these position differences are displayed in Figure 4, and the related RMS statistics are listed in Tables 3 and 4. Accordingly, the BDS-3 TCI solutions when applying real-time products from the CAS and WHU were mainly at the equal accuracy grade as those using the final products. The differences among the positions calculated based on the CAS, WHU, and final products are 0.058 m, 0.057 m, and 0.079 m in light of the RMSs in the east, north, and up components. It can be observed that the position solution applied to the CAS real-time products succeeds with the highest accuracy (0.383 m, 0.476 m, and 0.790 m) in comparison with the results that adopt the other three real-time products. Visibly, the results of DLR product-based solutions have the worst position accuracy, which are 1.576 m, 0.766 m, and 1.414 m in the three directions. This is because the DLR real-time products do not provide the orbit and clock corrections of BDS-3 IGSO, which leads to the total number of available satellites being 2–3 fewer than that of other schemes and results in a higher PDOP value (as shown in Figure 5). For the GPS TCI results, the position errors calculated by applying the real-time products from the four ACs were poorer than those of the final precision products, most notably in the vertical component.

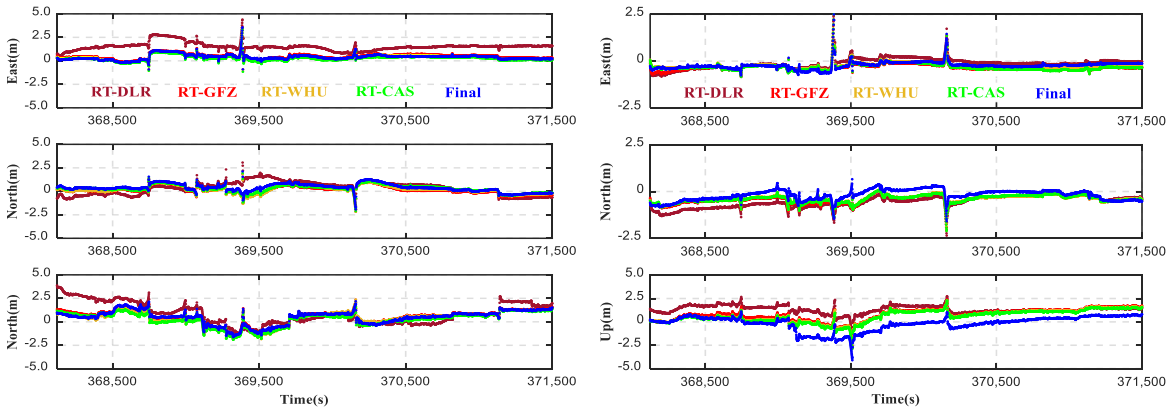

Figure 4. Position differences of BDS-3 PPP/INS TCI (**a**) and GPS PPP/INS TCI (**b**) with different orbit and clock products.

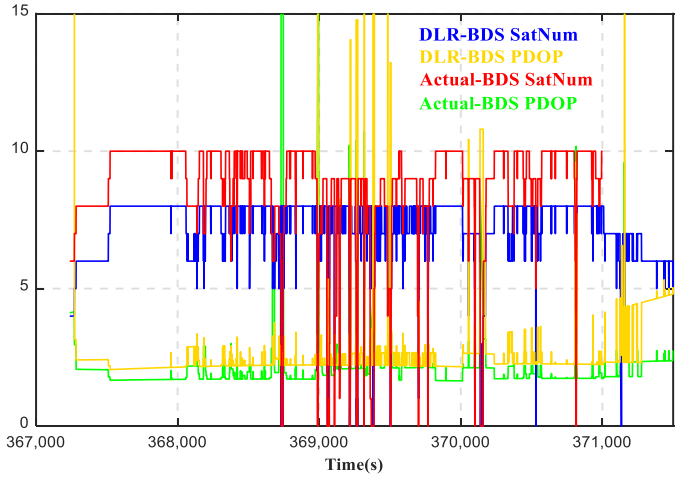

Figure 5. Satellite numbers and PDOP values with DLR products.

The Cumulative Distribution Functions (CDFs) of BDS-3/GPS TCI position errors are displayed in Figure 6. The CDFs of BDS-3 TCI positioning errors calculated by different orbit and clock products also prove that the position solutions using the CAS and WHU products are roughly the same as those taking advantage of the final products. The results with using the products of GFZ and DLR are worse, especially in the east and vertical directions. Moreover, it is visible from the CDF of GPS TCI that the position errors of the final precision products were better than those of the real-time products from the four ACs.

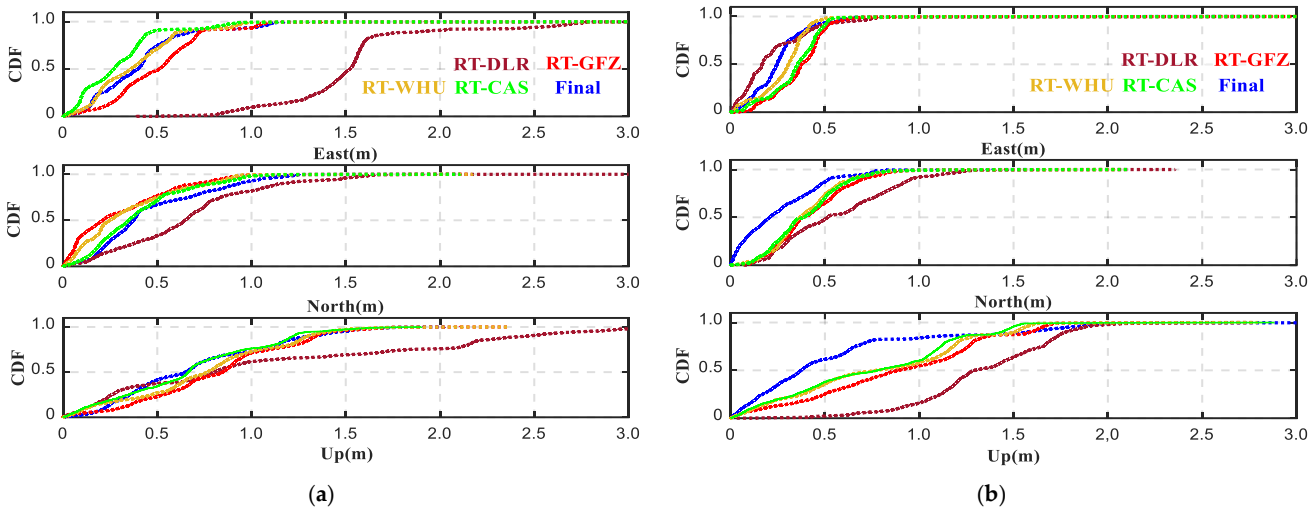

Figure 6. Position error CDF of BDS-3 PPP/INS TCI (**a**) and GPS PPP/INS TCI (**b**) with different orbit and clock products.

4.2. Impacts of Doppler Observation on PPP/INS Integration

Data processing was carried out in two modes: BDS-3/GPS TCI-dmode0 (with Doppler) and BDS-3/GPS TCI-dmode1 (without Doppler) to analyze the impact of Doppler observation on positioning, velocity, and attitude determination of PPP/INS tight integration. Table 5 lists the corresponding RMSs of position, velocity, and attitude of the BDS-3/GPS TCI. Based on statistics, the horizontal and vertical position accuracy of BDS-TCI-dmode0 and BDS-TCI-dmode1 are similar, and the discrepancies are within 1 cm. The accuracies of velocity and attitude in modes of dmode0 and dmode1 are virtually unanimous. Here, the differences in velocity RMS are less than 1 cm/s, and these in attitude are less than 0.01°. Similar results are also found in the GPS TCI-based schemes. Accordingly,

it can be seen that the impact of Doppler observation on the overall positioning, velocity, and attitude determination is invisible.

Table 5. RMS of position, velocity, and attitude of BDS-3/GPS TCI in modes of dmode0 and dmode1.

Mode	Position (m)			Velocity (cm/s)			Attitude (°)		
	East	North	Up	East	North	Up	Roll	Pitch	Heading
BDS-TCI-dmode0 [1]	0.406	0.419	0.782	1.88	2.04	3.16	0.276	1.319	0.502
BDS-TCI-dmode1 [2]	0.408	0.419	0.788	1.90	2.17	3.16	0.276	1.321	0.503
GPS-TCI-dmode0 [1]	0.305	0.372	0.758	1.69	2.04	3.06	0.275	1.314	0.506
GPS-TCI-dmode1 [2]	0.301	0.387	0.759	1.72	2.46	3.06	0.276	1.318	0.505

[1] TCI-dmode0 indicates TCI with Doppler; [2] TCI-dmode1 indicates TCI without Doppler.

According to Equations (5) and (7), Doppler observations could provide enhancements for the estimation of position, velocity, and attitude. Therefore, the impacts of Doppler observations on the initial convergence speed of position, velocity, and attitude (the first 100 s) were further analyzed.

Figure 7 displays the position offsets of BDS-3/GPS TCI-dmode0 and TCI-dmode1 in the east, north, and up components. The average position errors are also presented in Table 6. It is noticeable that the vertical position offsets on the initial epochs have been improved with the assistance of Doppler observations in both BDS-3 TCI and GPS TCI. Following the statistics, the average position error is upgraded from 0.744 m and 0.777 m in BDS-3 TCI-dmode1 to 0.286 m and 0.650 m in BDS-3 TCI-dmode0, with an improvement of 61.6% and 16.3% in the east and north directions. For the GPS TCI solution, there are 63.2% enhancements in the up direction. In addition, the max position errors of the BDS-3/GPS TCI in modes of dmode0 and dmode1 are present in Figure 8. It becomes apparent that Doppler observation has a significant effect on the position results, especially in the east component. The improvement from Doppler observations of BDS-3 and GPS are 68.8% and 68.4% in the east direction.

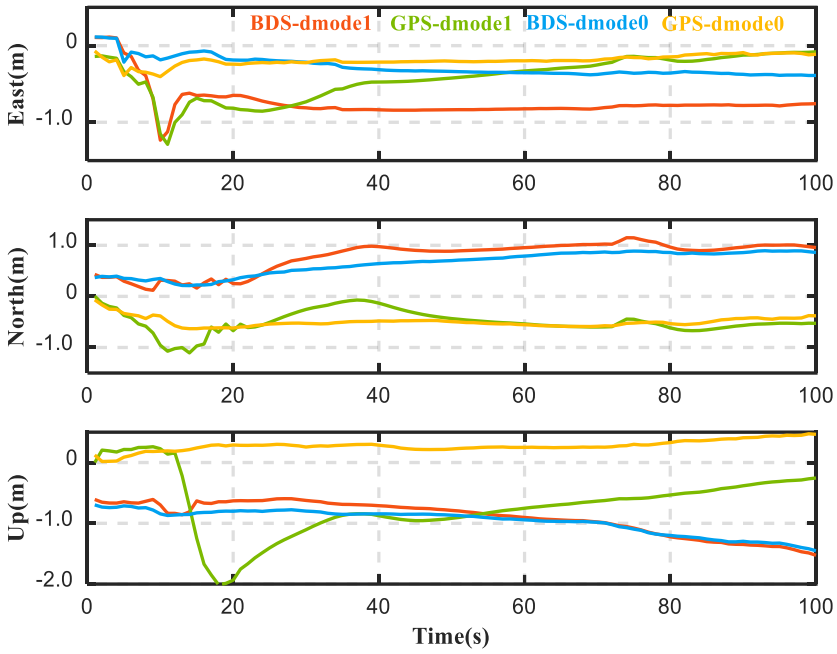

Figure 7. Position offsets of the BDS-3/GPS TCI in modes of dmode0 (with Doppler) and dmode1 (without Doppler).

Table 6. Average errors of position, velocity, and attitude of BDS-3/GPS TCI with and without Doppler observation in initial 100 s.

Mode	Position (m)			Velocity (cm/s)			Attitude (°)		
	East	North	Up	East	North	Up	Roll	Pitch	Heading
BDS-TCI-dmode0 [1]	0.286	0.650	0.966	4.15	6.11	1.09	0.364	1.869	6.626
BDS-TCI-dmode1 [2]	0.744	0.777	0.904	18.01	11.04	2.65	0.619	1.835	12.667
GPS-TCI-dmode0 [1]	0.192	0.499	0.275	4.45	5.96	1.46	0.384	1.851	6.837
GPS-TCI-dmode1 [2]	0.419	0.496	0.748	27.49	11.60	4.44	0.761	1.834	13.861

[1] TCI-dmode0 indicates TCI with Doppler; [2] TCI-dmode1 indicates TCI without Doppler.

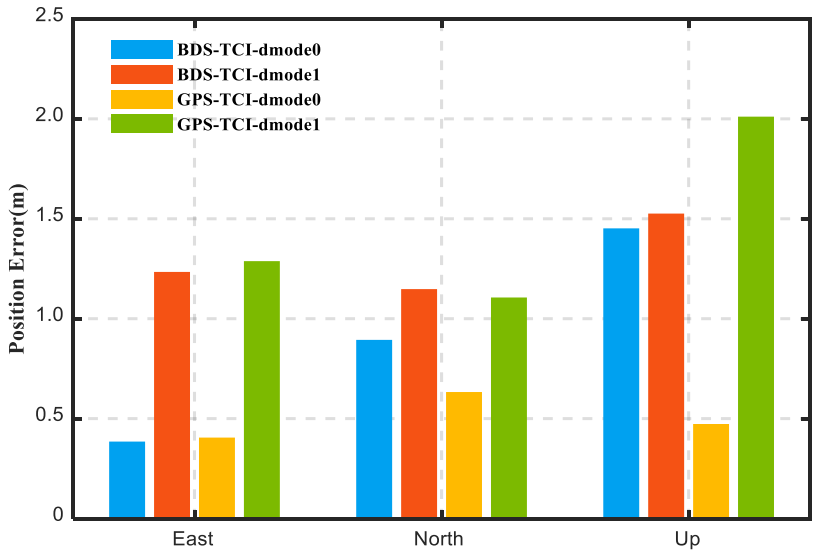

Figure 8. The max position errors of the BDS-3/GPS TCI in modes of dmode0 (with Doppler) and dmode1 (without Doppler).

Shown in Figure 9 are the velocity offsets sequences of BDS-3/GPS TCI-dmode0 and TCI-dmode1 in the east, north, and up components, and the velocity errors on average are presented in Table 6. The results show that the velocity offsets on the initial epochs have been significantly improved with the assistance of Doppler observations in both BDS-3 TCI and GPS TCI. According to the statistic in Table 6, the average velocity errors are improved from 18.01 cm/s, 11.04 cm/s, and 2.65 cm/s in BDS-3 TCI-dmode1 to 4.15 cm/s, 6.11 cm/s, and 1.06 cm/s in BDS-3 TCI-dmode0, with improvements of 76.9%, 44.8%, and 60.0% in the east, north, and up directions. With regards to the GPS TCI case, the enhancements from TCI-dmode0 are 83.8% and 48.9%, and 67.1% in east, north, and up components by comparison with the results from TCI-dmode1. Visibly, the initial convergence time is shortened in the PPP/INS TCI with Doppler observations. Moreover, Figure 10 presents the max velocity errors of the BDS-3/GPS TCI in modes of dmode0 and dmode1, respectively. It is noticeable that the max velocity errors of both BDS-3 TCI and GPS TCI in dmode0 decrease significantly compared to the results in dmode1. The max velocity errors of the BDS-3 TCI-dmode1 decrease from 77.5 cm/s, 102.4 cm/s, and 20.3 cm/s in the east, north, and vertical directions to 31.2 cm/s, 33.9 cm/s, and 7.1 cm/s, with improvements of 59.7%, 66.9%, and 65.0%, respectively. Similarly, the max velocity errors of GPS TCI-dmode1 are improved from 152.7 cm/s, 114.8 cm/s, and 28.1 cm/s to 36.7 cm/s, 30.3 cm/s, and 11.5 cm/s, respectively, with an enhancement of approximately 75.9%, 73.6%, and 59.1% in the three directions, respectively.

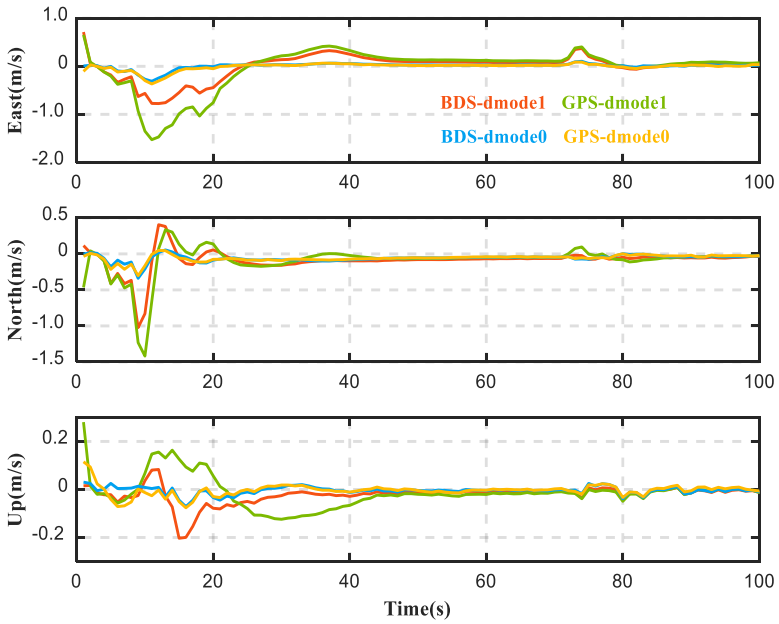

Figure 9. Velocity offsets of the BDS-3/GPS TCI in modes of dmode0 (with Doppler) and dmode1 (without Doppler).

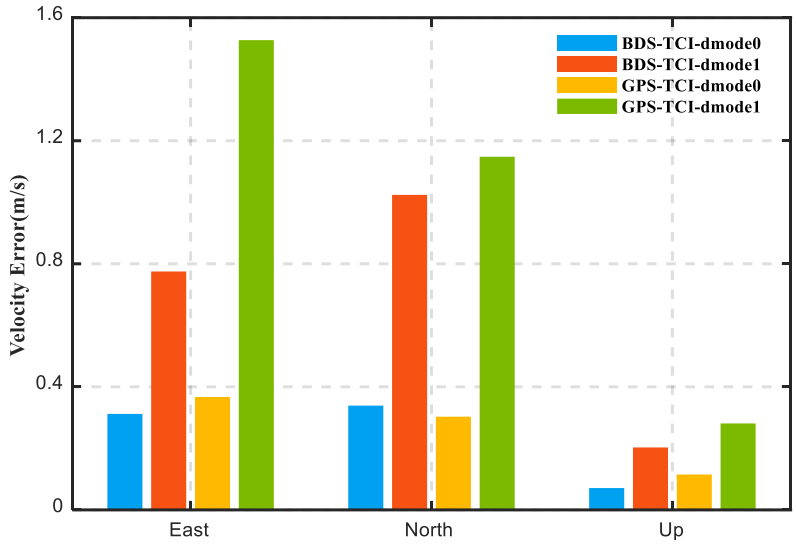

Figure 10. The max velocity errors of the BDS-3/GPS TCI in modes of dmode0 (with Doppler) and dmode1 (without Doppler).

Figure 11 presents the offsets of roll, pitch, and heading angles from BDS-3/GPS TCI in modes of dmode0 and dmode1, and the related average errors are exhibited in Table 6. It is noteworthy that the attitude errors of roll and heading calculated by the dmode0 mode show visible enhancements on the initial epochs compared to those of dmode1. Following the statistics presented in Table 6, the average errors of roll and heading are 0.619° and 12.667° in BDS TCI-dmode1. While applying Doppler observations, the corresponding errors are upgraded to 0.364° and 6.636°. For the GPS-based solutions, Doppler observations bring 49.5% and 50.7% enhancements in roll and heading. Additionally, the maximum errors of pitch, roll, and heading of these modes are presented in Figure 12, which illustrates the accuracy upgradation in pitch. It is also significant that the maximum error of heading is much larger than that of roll and pitch, which is due to that the gyro has weak observability in the vertical axis.

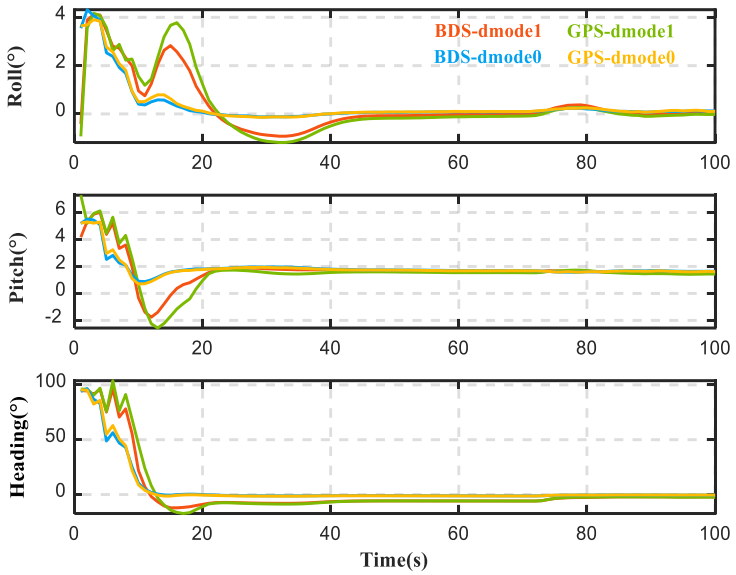

Figure 11. Attitude offsets of the BDS-3/GPS TCI in modes of dmode0 (with Doppler) and dmode1 (without Doppler).

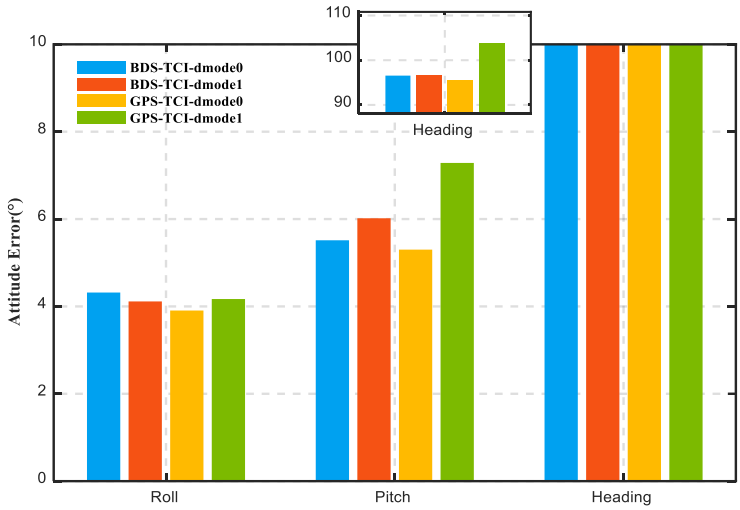

Figure 12. The max attitude errors of the BDS-3/GPS TCI in modes of dmode0 (with Doppler) and dmode1 (without Doppler).

The initial convergence time of position, velocity, and attitude are further evaluated. Figure 13 displays the average and max convergence time of the BDS-3/GPS TCI in modes of dmode0 (with Doppler) and dmode1 (without Doppler). In this study, the velocity and attitude convergence time is defined as the time required to keep the error less than the average errors of dmode0 in each component (as shown in Table 6). The convergence time of position is defined as the time required to keep the horizontal error stabilized. The max and average convergence times among each component are displayed. Apparently, the initial convergence time of position, velocity, and attitude are shortened in the PPP/INS TCI with Doppler observations, and such improvements are more evident in the convergence of velocity and attitude. For the results of BDS-TCI, there are 53.2% and 68.2% enhancements in the average convergence time of velocity and attitude. With the assistance of Doppler observations, the convergence of velocity and attitude components can be achieved in less than 50 s and 20 s. A relatively stable position accuracy can be reached within 100 s. Accordingly, it can be concluded that Doppler observations have positive influences on the initial convergence speed of velocity and attitude.

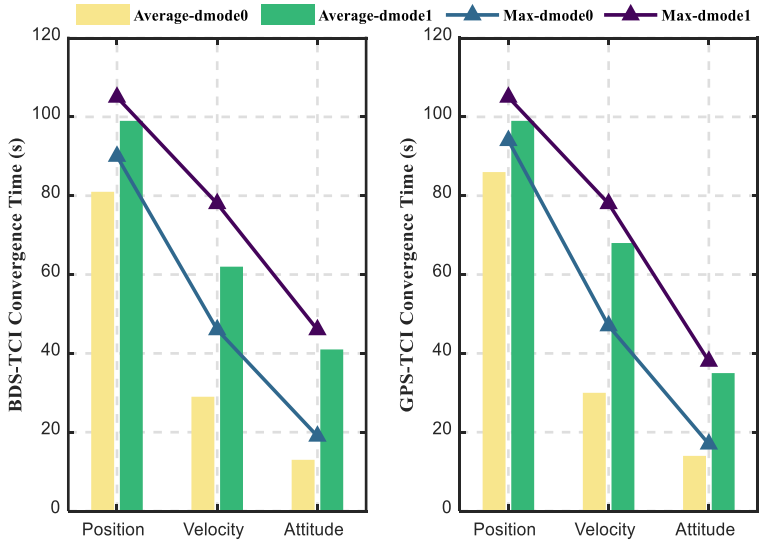

Figure 13. Average and max convergence time of the BDS-3 TCI (**left**) and GPS TCI (**right**) in modes of dmode0 (with Doppler) and dmode1 (without Doppler) during initial convergence.

Moreover, we further analyze the influence of Doppler observations on BDS-3 TCI during reconvergence periods (as pointed by black arrows in Figure 2). The position, velocity, and attitude error during the initial 20 s are evaluated. Figure 14 shows the average error of position, velocity, and attitude during these reconvergence periods. The results display that the improvements of average position errors from TCI-dmode0 are 46.5%, 8.1%, and 67.1% in the east, north, and up by comparison with the results from TCI-dmode1. As for average velocity errors, there are 52.7%, 29.2%, and 50.6% enhancements in the three directions. Meanwhile, the improvement in heading is 24.7%, while there are no significant improvements in roll and pitch. The effect of Doppler observations on attitude error during reconvergence is less conspicuous, which is because the divergence of attitude error is smaller than the velocity and position during the short outages of satellite signals. According to Equation (20), the attitude error diverges with the first power of time, while the velocity and position diverge with the quadratic and cubic of time. However, it is noticeable that Doppler observations have visible improvements to the position and velocity errors during the reconvergence period.

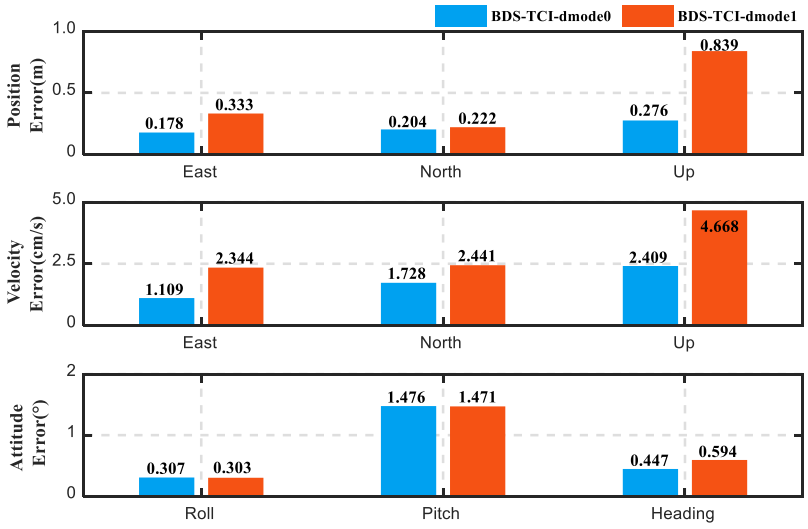

Figure 14. Average errors of the BDS-3 TCI in modes of dmode0 (with Doppler) and dmode1 (without Doppler) during reconvergence.

4.3. Impacts of IMU Data Interval on PPP/INS Integration

The position differences of BDS-3/GPS PPP/INS tight integration calculated by three types of rates (100 Hz, 50 Hz, and 10 Hz) of IMU data are shown in Figure 15. The position accuracies in terms of RMS values are listed in Tables 7 and 8. Significantly, the position RMSs using 100 Hz IMU data are 0.406 m, 0.419 m, and 0.782 m in the east, north, and vertical components. While using IMU measurements at 50 Hz, the position accuracy has no significant differences by comparison with the solutions at 100 Hz. However, the position RMSs have degradations of 0.192 m, 0.062 m, and 0.052 m when reducing the IMU data sampling rate to 10 Hz. A similar conclusion can also be obtained from the GPS-based solutions. The CDF of BDS-3/GPS TCI position error by using three types of IMU data is given in Figure 16, which proves that the position accuracy is not associated with the IMU data rate. This is because the absolute positioning accuracy of PPP/INS TCI mainly depends on PPP.

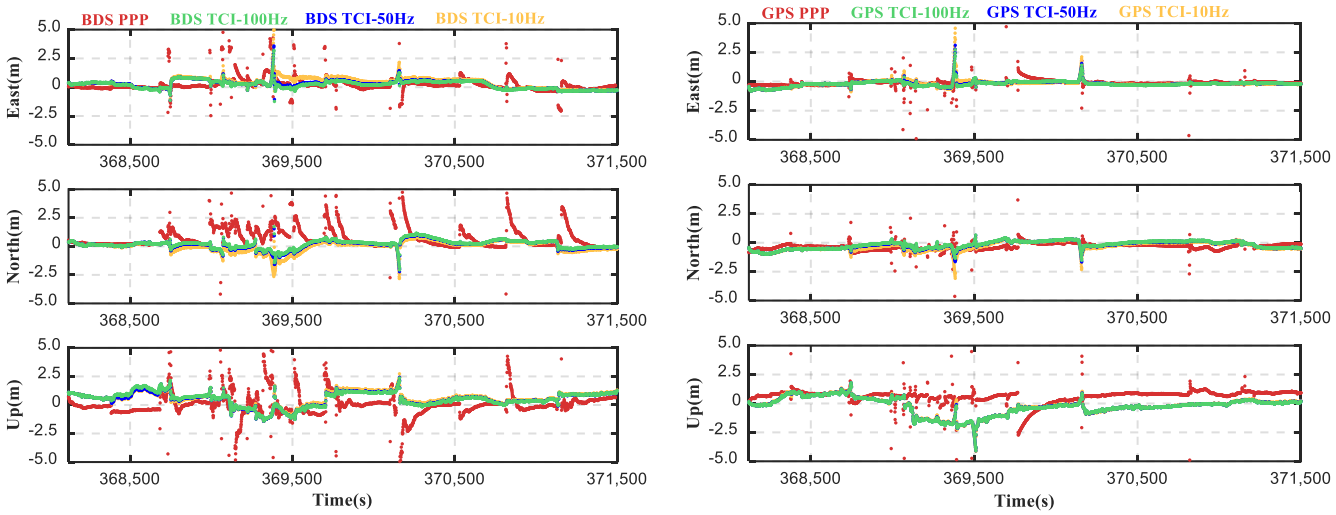

Figure 15. Position differences of BDS-3 PPP/INS TCI (**a**) and GPS PPP/INS TCI (**b**) by using three types of IMU data (100 Hz, 50 Hz, and 10 Hz).

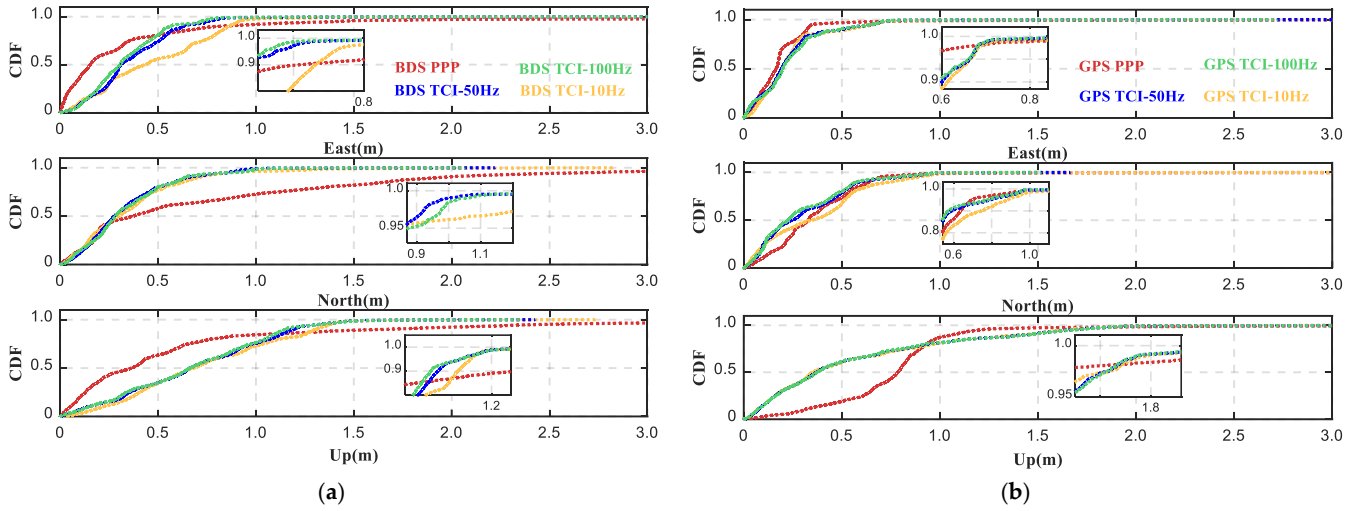

Figure 16. Position error CDF of BDS-3 PPP/INS TCI (**a**) and GPS PPP/INS TCI (**b**) by using three types of IMU data (100 Hz, 50 Hz, and 10 Hz).

Table 7. RMS of BDS-3 PPP and TCI position, velocity, and attitude.

Mode	Position (m)			Velocity (cm/s)			Attitude (°)		
	East	North	Up	East	North	Up	Roll	Pitch	Heading
PPP	0.882	1.361	1.311						
TCI-100 HZ	0.406	0.419	0.782	1.88	2.04	3.16	0.276	1.319	0.502
TCI-50 HZ	0.438	0.415	0.791	2.17	2.28	3.29	0.275	1.324	0.504
TCI-10 HZ	0.598	0.481	0.834	3.38	3.38	4.27	0.278	1.443	0.528

Table 8. RMS of GPS PPP and TCI position, velocity, and attitude.

Mode	Position (m)			Velocity (cm/s)			Attitude (°)		
	East	North	Up	East	North	Up	Roll	Pitch	Heading
PPP	0.586	0.539	0.984						
TCI-100 HZ	0.305	0.372	0.758	1.69	2.04	3.06	0.275	1.314	0.506
TCI-50 HZ	0.309	0.388	0.773	2.01	2.31	3.21	0.275	1.319	0.508
TCI-10 HZ	0.349	0.476	0.774	3.33	3.45	4.22	0.277	1.436	0.529

In addition, we also investigated the performance of velocity and attitude determination using IMU data at different sampling rates. Figures 17 and 18 present the velocity and attitude errors in the time sequence, respectively. The related RMSs are shown in Tables 7 and 8. Significantly, the accuracies of velocity are degraded by using IMU data at a lower rate (50 Hz and 10 Hz). According to the statistics, the velocity accuracies at 10 Hz are the lowest. The velocity RMSs of BDS-3 TCI are 3.38 cm/s, 3.38 cm/s, and 4.27 cm/s in the east, north, and up components, and those of GPS TCI are 3.33 cm/s, 3.45 cm/s, and 4.22 cm/s. The accuracies of attitude do not show a visible distinction between the solutions based on the IMU data at 100 Hz and 50 Hz, but the accuracy degradation is significant while using 10 Hz IMU data. To display the impact of the IMU sampling rate on velocity and attitude results more clearly, the CDFs of BDS-3/GPS TCI velocity and attitude errors are given in Figures 19 and 20. It can be found that the accuracy of both velocity and attitude are significantly decreased when using the IMU data rate at 10 Hz.

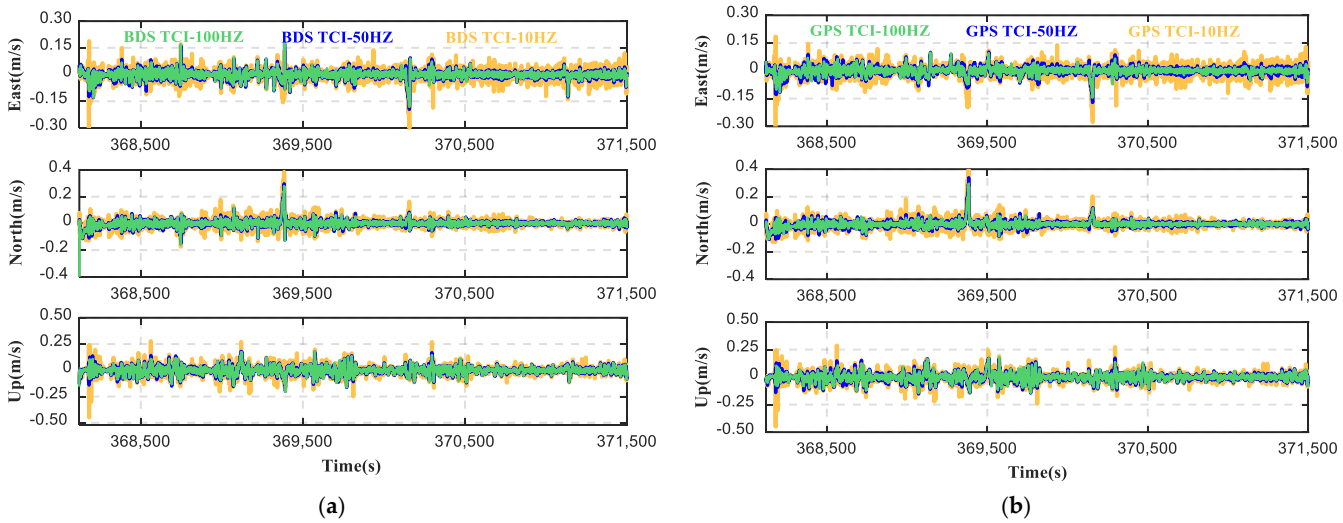

Figure 17. Velocity differences of BDS-3 PPP/INS TCI (**a**) and GPS PPP/INS TCI (**b**) by using three types of IMU data (100 Hz, 50 Hz, and 10 Hz).

To further investigate the performance of PPP/INS tightly coupled integration in complex conditions, we simulated two 30 s partial satellite signal outages at 368,500 s and 370,500 s. It should be noted that only three satellites were available at the time of the partial outage period. Simultaneously, IMU data with different sampling rates (100 Hz,

50 Hz, and 10 Hz) were processed to further explore the impacts of IMU sampling rates on PPP/INS TCI under challenging GNSS environments. The corresponding position results are given in Figure 21. It is noticeable that the position drifts of PPP/INS TCI diverge along with outage time. The BDS-3 TCI position RMS values, while using 100 Hz IMU data, are degraded to 0.875 m, 2.258 m, and 5.210 m in the east, north, and vertical directions, while partial outage time lasts to 30 s. While using 50 Hz IMU data, the position drifts after a 30 s outage are 0.839 m, 2.185 m, and 5.140 m in three directions. The position drifts are slightly restrained while using IMU data at 50 Hz. The position drifts using 10 Hz IMU data are 0.689 m, 1.877 m, and 4.796 m in the three directions. Similar results can also be found in the results of GPS-based solutions. This shows that the IMU sampling rate affects position offsets of PPP/INS TCI when there are partial satellite outages. In general, for this consumer-grade IMU (INS616), it is equivalent to reducing IMU sensor cumulative errors (white noise and unmodeled errors) by reducing INS mechanization frequency while downsampling the IMU data rate.

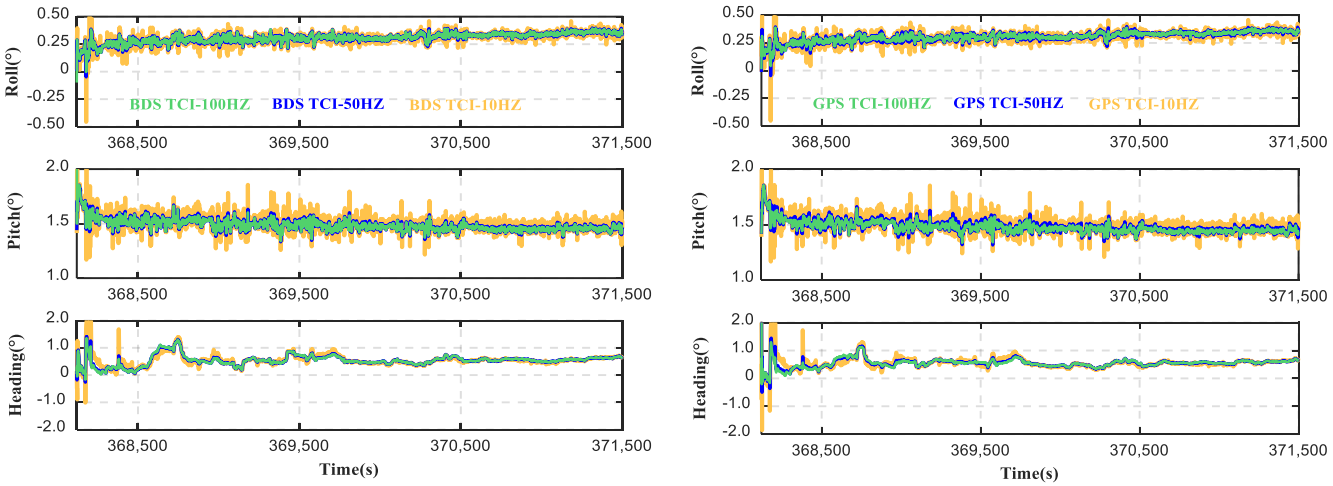

Figure 18. Attitude differences of BDS-3 PPP/INS TCI (**a**) and GPS PPP/INS TCI (**b**) by using three types of IMU data (100 Hz, 50 Hz, and 10 Hz).

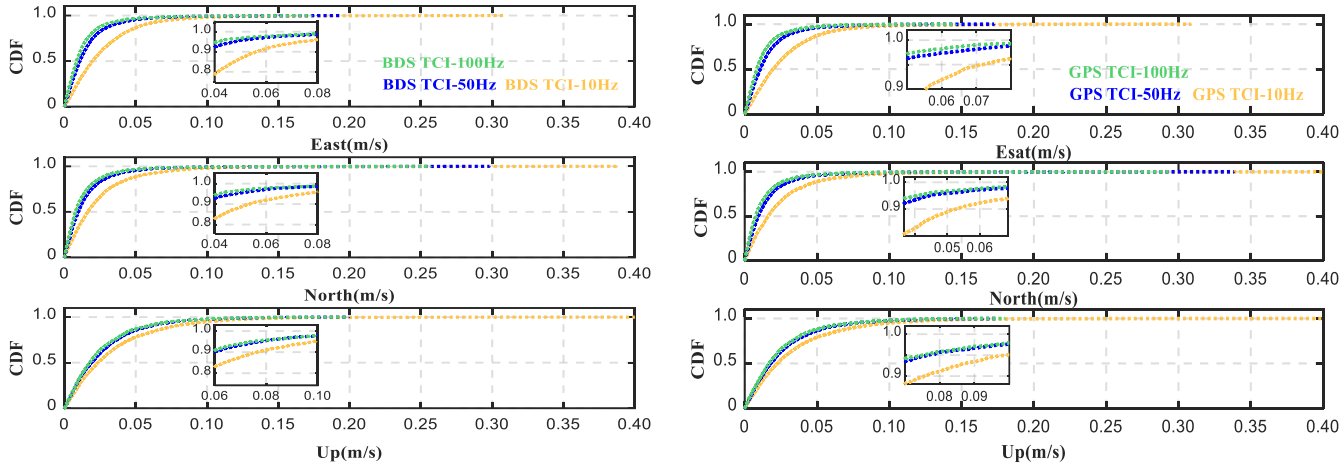

Figure 19. Velocity error CDF of BDS-3 PPP/INS TCI (**a**) and GPS PPP/INS TCI (**b**) by using three types of IMU data (100 Hz, 50 Hz, and 10 Hz).

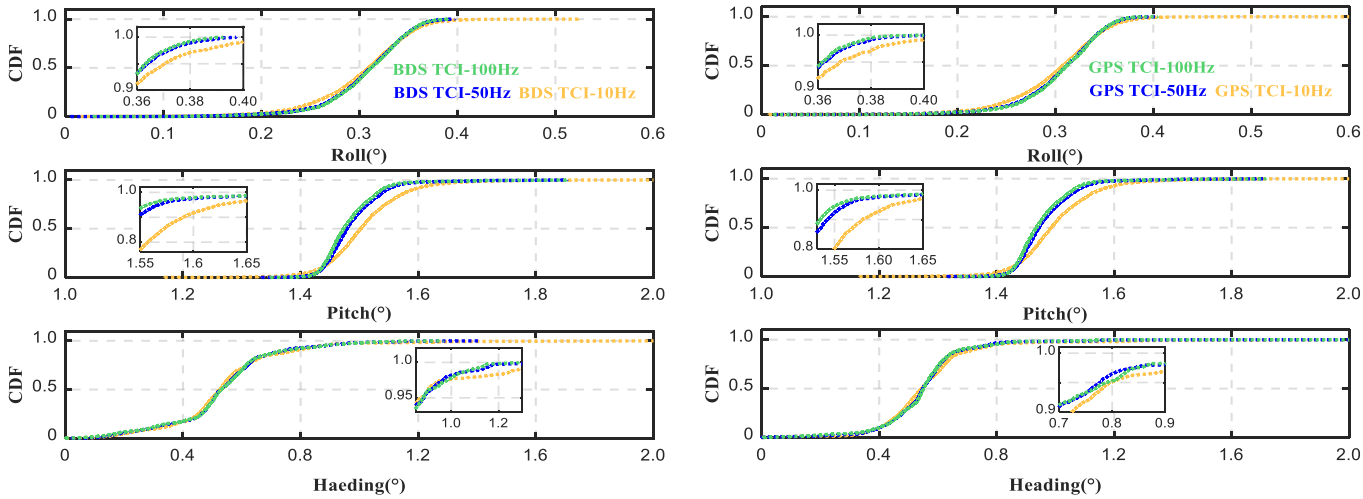

Figure 20. Attitude error CDF of BDS-3 PPP/INS TCI (**a**) and GPS PPP/INS TCI (**b**) by using three types of IMU data (100 Hz, 50 Hz, and 10 Hz).

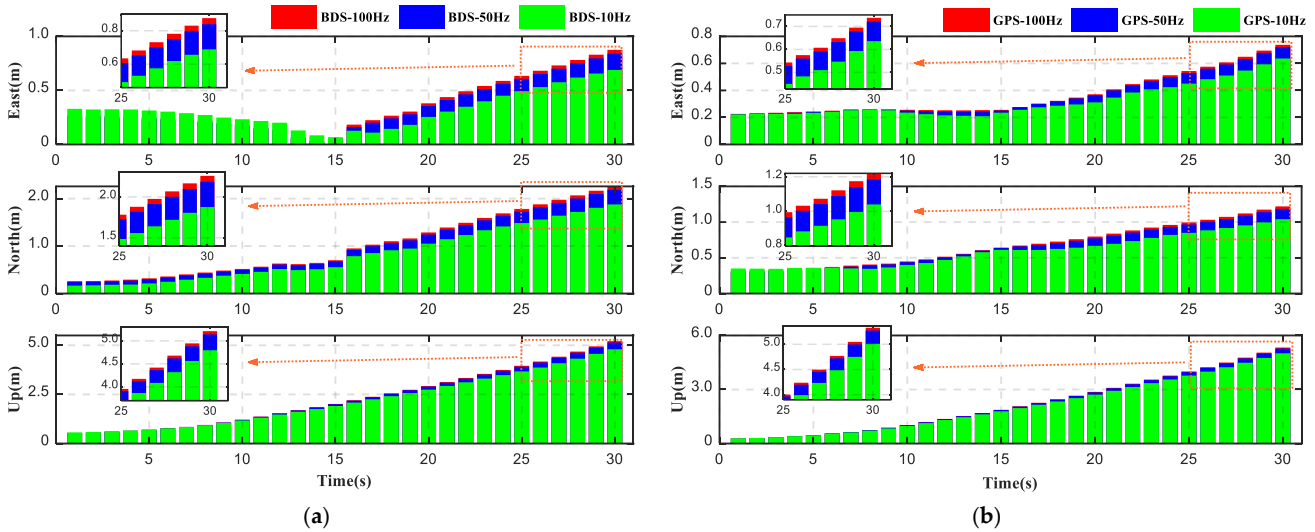

Figure 21. RMSs of position drifts computed by BDS PPP/INS TCI (**a**) and GPS PPP/INS TCI (**b**) using three types of IMU data with different sampling rates in the GNSS outage simulation test.

Moreover, this set of vehicle-borne data was collected in complex urban environments, and there were frequent signal outages happening during the experiment. To further investigate the effect of IMU data rate on TCI during complete satellite signal outage, we analyzed the position drifts over these complete outage periods. Specifically, two sets of 15 s complete satellite signal outages were analyzed as examples. BDS-3/GPS TCI position drifts calculated by three types of IMU data (100 Hz, 50 Hz, and 10 Hz) during the complete outages are given in Figure 22. The BDS-3 TCI position drifts while using 100 Hz IMU data are 0.555 m, 0.832 m, and 1.281 m in the east, north, and vertical directions while complete outage time lasts to 15 s. With reducing the IMU sampling rate, the position drifts are increased. Among the results calculated from different IMU rate data, the maximum position drifts using 50 Hz IMU data are 0.713 m, 0.949 m, and 1.302 m, and those using 10 Hz IMU data are 1.305 m, 1.338 m, and 1.375 m, respectively. It is also notable that the position drifts using different IMU data are more distinct in the east and north directions than in the vertical direction. The position error divergence over complete outages is not consistent with the result during partial satellite signal outages. The reasons may be as follows. According to Equation (21), the bias and scale factor error are described as the

first-order Gauss–Markov process. When there are GNSS signals, the first part can be offset by IMU error compensation. The rest is the white noise, which can become a random walk process after integration. The state uncertainty of the random walk process increases with time. Thus, with the decreasing of the IMU sampling rate, the INS mechanization frequency is reduced, and so are the cumulative errors. However, when GNSS signals are completely out, x_{k-1} of the first part maintains the previous value with GNSS signals. The error of the first part is smaller at a smaller time interval when the IMU data rate is higher.

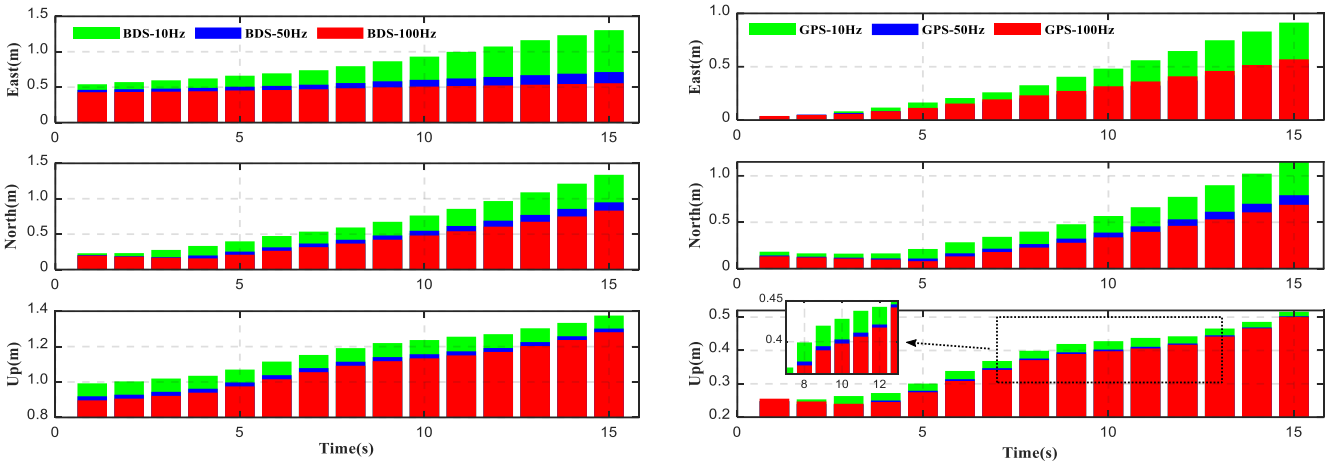

(**a**) (**b**)

Figure 22. RMSs of position drifts computed by BDS-3 PPP/INS TCI (**a**) and GPS PPP/INS TCI (**b**) using three types of IMU data with different sampling rates in the GNSS complete outage.

5. Conclusions

This paper implemented the tightly coupled integration of BDS-3 PPP and low-cost INS through the RKF algorithm. The corresponding mathematical models were described, and the performance was assessed through a land vehicular field trial. The results are evaluated from the perspectives of (1) the impacts of real-time orbit and clock products from different ACs (the CAS, DLR, GFZ, and WHU) on PPP/INS integration; (2) the impact of the robust algorithm on PPP/INS integration; (3) the impacts of Doppler observation on PPP/INS integration; and (4) the impacts of IMU data interval on PPP/INS integration.

According to the statistical results, the position results are slightly improved while adopting the RKF algorithm. The accuracy of orbit and clock products from different ACs is different, and it presents a direct impact on the solutions of PPP/INS integration. In the case of the BDS-based solutions, those with products from the CAS and WHU ACs are with higher accuracy, which is almost at the equal accuracy standard in comparison with those using the final products. However, the results of using GFZ and DLR products are poorer. Similar conclusions can also be found in the GPS-based solutions. In addition, Doppler observations present insignificant influence on the performance of the overall positioning, velocity, and attitude, whereas the accuracy of velocity and attitude in the initial convergence period is significantly improved with the assistance of Doppler observations, as well as the accuracy of position and velocity during reconvergence periods. Meanwhile, the impacts of IMU data interval on the performance of PPP/INS tight integration are inconspicuous when the satellite signals are available for PPP. However, the position drifts diverge together with the accumulative outage period, and the speed of such divergent processes are affected by the IMU sampling rate.

Author Contributions: Conceptualization, J.K. and Z.G.; data curation, J.K., Q.X. and R.L.; funding acquisition, C.Y. and J.L.; investigation, J.K. and Z.G.; software, Z.G.; visualization, C.Y. and J.L.; writing—original draft preparation, J.K.; writing—review and editing, J.K., Z.G. and J.L. All authors have read and agreed to the published version of the manuscript.

Funding: This research was partly supported by the National Key Research and Development Program of China (Grant No. 2021YFB3901301) and the National Natural Science Foundation of China (NSFC) (Grant No. 42274022).

Institutional Review Board Statement: Not applicable.

Informed Consent Statement: Not applicable.

Data Availability Statement: The datasets adopted in this paper are managed by the School of Land Science and Technology, China University of Geosciences Beijing, and can be available on request from the corresponding author.

Acknowledgments: The authors would like to thank anonymous reviewers who gave us valuable suggestions that have helped to improve the quality of the manuscript.

Conflicts of Interest: The authors declare no conflict of interest.

References

1. Zumberge, J.F.; Heflin, M.B.; Jefferson, D.C.; Watkins, M.M.; Webb, F.H. Precise point positioning for the efficient and robust analysis of GPS data from large networks. *J. Geophys. Res. Solid Earth* **1997**, *102*, 5005–5017. [CrossRef]
2. Malys, S.; Jensen, P.A. Geodetic point positioning with GPS carrier beat phase data from the CASA UNO experiment. *Geophys. Res. Lett.* **1990**, *17*, 651–654. [CrossRef]
3. Xun, S. *GPS Measurement Principle and Application*; Wuhan University Press: Wuhan, China, 2003.
4. Kouba, J.; Héroux, P. Precise Point Positioning Using IGS Orbit and Clock Products. *GPS Solut.* **2001**, *5*, 12–28. [CrossRef]
5. Elsobeiey, M.; Al-Harbi, S. Performance of Real-Time Precise Point Positioning Using IGS Real-Time Service. *GPS Solut.* **2016**, *20*, 565–571. [CrossRef]
6. Xia, F.; Ye, S.; Zhao, L.; Hu, G. Analysis of Real-time Precise Point Positioning Based on SSR Corrections. *Navig. Position. Timing* **2017**, *4*, 52–57.
7. Weber, G.; Mervart, L.; Lukes, Z.; Rocken, C.; Dousa, J. Real-time clock and orbit corrections for improved point positioning via NTRIP. In Proceedings of the ION GNSS 20th International Technical Meeting of the Satellite Division (ION GNSS 2007), Fort Worth, TX, USA, 25–28 September 2007; pp. 1992–1998.
8. Caissy, M.; Agrotis, L.; Weber, G.; Hernandez-Pajares, M.; Hugentobler, U. Coming soon: The international GNSS real-time service. *GPS World* **2012**, *23*, 52–58.
9. Hadas, T.; Bosy, J. IGS RTS Precise Orbits and Clocks Verification and Quality Degradation over Time. *GPS Solut.* **2015**, *19*, 93–105. [CrossRef]
10. Wang, L.; Li, Z.; Ge, M.; Neitzel, F.; Wang, X.; Yuan, H. Investigation of the performance of real-time BDS-only precise point positioning using the IGS real-time service. *GPS Solut.* **2019**, *23*, 66. [CrossRef]
11. Wang, W.; Yu, W.; Zeng, Q.; Wu, R. Assessment of CNES real-time orbit and clock product. In Proceedings of the 10th China Satellite Navigation Conference, Beijing, China, 22–25 May 2019.
12. Kazmierski, K.; Zajdel, R.; Sośnica, K. Evolution of Orbit and Clock Quality for Real-Time Multi-GNSS Solutions. *GPS Solut.* **2020**, *24*, 111. [CrossRef]
13. Wang, Z.; Li, Z.; Wang, L.; Wang, X.; Yuan, H. Assessment of Multiple GNSS Real-Time SSR Products from Different Analysis Centers. *Int. J. Geo-Inf.* **2018**, *7*, 85. [CrossRef]
14. Li, W.; Kacmarik, M. Assessment of Multi-GNSS Precise Orbit and Clock Products from Different Analysis Centers Based on Precise Point Positioning. *Acta Geodyn. Geomater.* **2021**, *18*, 387–397. [CrossRef]
15. Weiss, J.D.; Kee, D.S. A Direct Performance Comparison Between Loosely Coupled and Tightly Coupled GPS/INS Integration Techniques. In Proceedings of the 51st Annual Meeting of The Institute of Navigation 1995, Colorado Springs, CO, USA, 5–7 June 1995; pp. 537–544.
16. Kjørsvik, N.S.; Gjevestad, J.G.; Brøste, E.; Gade, K.; Hagen, O.K. Tightly Coupled Precise Point Positioning and Inertial Navigation Systems. In Proceedings of the International Society for Photgrammetry and Remote Sensing European Calibration and Orientation Workshop, Casteldefels, Spain, 10–12 February 2010.
17. Gao, Z.; Ge, M.; Shen, W.; Li, Y.; Chen, Q.; Zhang, H.; Niu, X. Evaluation on the Impact of IMU Grades on BDS + GPS PPP/INS Tightly Coupled Integration. *Adv. Space Res.* **2017**, *60*, 1283–1299. [CrossRef]
18. Shin, E.; Scherzinger, B. Inertially Aided Precise Point Positioning. In Proceedings of the 22nd International Technical Meeting of the Satellite Division of The Institute of Navigation (ION GNSS 2009), Savannah, GA, USA, 22–25 September 2009; pp. 1892–1897.
19. Roesler, G.; Martell, H. Tightly coupled processing of precise point position (PPP) and INS data. In Proceedings of the 22nd International Meeting of the Satellite Division of the Institute of Navigation, Savannah, GA, USA, 22–25 September 2009.

20. Falco, G.; Pini, M.; Marucco, G. Loose and tight GNSS/INS integrations: Comparison of performance assessed in real urban scenarios. *Sensors* **2017**, *17*, 255. [CrossRef]
21. Du, S. Integration of Precise Point Positioning and Low-Cost MEMS IMU. Ph.D. Dissertation, University of Calgary, Calgary, AB, Canada, 2010.
22. Abd Rabbou, M.; El-Rabbany, A. Tightly Coupled Integration of GPS Precise Point Positioning and MEMS-Based Inertial Systems. *GPS Solut.* **2015**, *19*, 601–609. [CrossRef]
23. Gao, Z.; Zhang, H.; Ge, M.; Niu, X.; Shen, W.; Wickert, J.; Schuh, H. Tightly Coupled Integration of Multi-GNSS PPP and MEMS Inertial Measurement Unit Data. *GPS Solut.* **2017**, *21*, 377–391. [CrossRef]
24. Elmezayen, A.; El-Rabbany, A. Ultra-Low-Cost Tightly Coupled Triple-Constellation GNSS PPP/MEMS-Based INS Integration for Land Vehicular Applications. *Geomatics* **2021**, *1*, 258–286. [CrossRef]
25. Sun, Y.; Li, Z.; Yang, Z.; Shao, K.; Chen, W. Motion Model-Assisted GNSS/MEMS-IMU Integrated Navigation System for Land Vehicle. *GPS Solut.* **2022**, *26*, 131. [CrossRef]
26. Elmezayen, A.; El-Rabbany, A. Performance Evaluation of Real-Time Tightly-Coupled GNSS PPP/MEMS-Based Inertial Integration Using an Improved Robust Adaptive Kalman Filter. *J. Appl. Geod.* **2020**, *14*, 413–430. [CrossRef]
27. Liu, X.; Li, D.; Shi, J.; Li, A.; Jiang, L. A Framework for Low-Cost Fusion Positioning with Single Frequency RTK/MEMS-IMU/VIO. *J. Phys. Conf. Ser.* **2021**, *1738*, 012007. [CrossRef]
28. Gonzalez, R.; Dabove, P. Performance Assessment of an Ultra Low-Cost Inertial Measurement Unit for Ground Vehicle Navigation. *Sensors* **2019**, *19*, 3865. [CrossRef]
29. Elsheikh, M.; Abdelfatah, W.; Noureldin, A.; Iqbal, U.; Korenberg, M. Low-Cost Real-Time PPP/INS Integration for Automated Land Vehicles. *Sensors* **2019**, *19*, 4896. [CrossRef] [PubMed]
30. Shao, K.; Li, Z.; Yang, Z.; Liu, Z.; Sun, Y. A Doppler Enhanced TDCP Algorithm Based on Terrain Adaptive and Robust Kalman Filter Using a Stand-Alone Receiver. *J. Navig.* **2022**, *75*, 864–877. [CrossRef]
31. He, K.; Xu, T.; Förste, C.; Wang, Z.; Zhao, Q.; Wei, Y. A Method to Correct the Raw Doppler Observations for GNSS Velocity Determination. In *International Association of Geodesy Symposia*; Springer: Berlin, Germany, 2022; pp. 1–6.
32. Liu, S.; Sun, F.; Chen, P. Research on DGPS/INS Tightly Coupled Algorithms Based on Pseudo-range and Doppler Observations. *Bull. Surv. Mapp.* **2013**, *6*, 5–8.
33. Liu, S.; Sun, F.; Zhang, L.; Li, W.; Zhu, X. Tight Integration of Ambiguity-Fixed PPP and INS: Model Description and Initial Results. *GPS Solut.* **2016**, *20*, 39–49. [CrossRef]
34. Wen, Z.C.; Li, Y.; Guo, X.L.; Zhang, X.X. Design and Evaluation of GNSS/INS Tightly-Coupled Navigation Software for Land Vehicles. *Int. Arch. Photogramm. Remote Sens. Spat. Inf. Sci.* **2022**, *46*, 213–218. [CrossRef]
35. Li, Z.; Yao, Y.; Wang, J.; Gao, J. Application of improved robust Kalman filter in data fusion for PPP/INS tightly coupled positioning system. *Metrol. Meas. Syst.* **2017**, *24*, 289–301. [CrossRef]
36. Du, Z.; Chai, H.; Xiao, G.; Xiang, M.; Yin, X.; Shi, M. The Realization and Evaluation of PPP Ambiguity Resolution with INS Aiding in Marine Survey. *Mar. Geod.* **2021**, *44*, 136–156. [CrossRef]
37. Zhou, B.; Zhang, W.; Rong, Y.; Hu, X.; Ma, J. Robust Adaptive Kalman Filtering Algorithm for Integrated Navigation Based on MEMS-INS/GNSS. *Navig. Control* **2018**, *17*, 14–20.
38. He, X.; Liu, C.; Chen, Y.; Ba, X.; Chen, J. Analysis of B2b signal of BDS III satellite. *Appl. Electron. Tech.* **2020**, *3*, 1–4.
39. Cheng, J.; Wang, W.; Ma, L.; Liu, W. Preliminary analysis of observation quality and positioning precision for BDS-3 satellites. *Bull. Surv. Mapp.* **2019**, *8*, 1–7.
40. Gao, Z. Research on the methodology and application of the integration between the multi-constellation GNSS PPP and inertial navigation system. Ph.D. Dissertation, Wuhan University, Wuhan, China, 2016.
41. Tu, R.; Ge, M.; Zhang, H.; Huang, G. The Realization and Convergence Analysis of Combined PPP Based on Raw Observation. *Adv. Space Res.* **2013**, *53*, 211–221. [CrossRef]
42. Gendt, G.; Dick, G.; Reigber, C.; Tomassini, M.; Liu, Y. Demonstration of NRT GPS water vapor monitoring for weather prediction in Germany. *J. Meteorol. Soc. Jpn.* **2003**, *82*, 360–370.
43. Shin, E.H. *Estimation Techniques for Low-Cost Inertial Navigation*; Library and Archives Canada: Ottawa, ON, Canada, 2006.
44. Brown, R.G.; Hwang, P.Y.C. *Introduction to Random Signals and Applied Kalman Filtering*; Willey: New York, NY, USA, 1992.
45. Yang, Y. *Adaptive Navigation and Kinematic Positioning*; Press of Surveying and Mapping: Beijing, China, 2006.
46. Yang, Y.; Song, L.; Xu, T. Robust Estimator for Correlated Observations Based on Bifactor Equivalent Weights. *J. Geod.* **2002**, *76*, 353–358. [CrossRef]